eng

MDPI

Article

Influence of La Geria-Inspired Microstructures (LGMs) on the Corrosion Behavior of Super Duplex Stainless Steel in Seawater and Desalination Brine Environments

Juan Carlos Lozano-Medina [1], Cristina Jiménez-Marcos [2,*], Amparo Verdu-Vazquez [3] and Julia Claudia Mirza-Rosca [2,4]

[1] Department of Processing Engineering, University of Las Palmas de Gran Canaria, 35017 Las Palmas de Gran Canaria, Spain; juancarlos.lozano@ulpgc.es
[2] Department of Mechanical Engineering, University of Las Palmas de Gran Canaria, 35017 Las Palmas de Gran Canaria, Spain; julia.mirza@ulpgc.es
[3] Building Technology Department, Madrid Polytechnic University, 28040 Madrid, Spain; amparo.verdu@upm.es
[4] Materials Engineering and Welding Department, Transilvania University of Brasov, 500036 Brasov, Romania
* Correspondence: cristina.jimenez112@alu.ulpgc.es

Abstract

Super duplex stainless steels are widely used in seawater desalination plants due to their high mechanical strength and excellent corrosion resistance in chloride-rich environments. However, during reverse osmosis processes, the salinity of the reject stream increases progressively, generating concentrated brines with concentrations close to 7 wt.% NaCl, which represent a chloride-rich service environment that may affect passive film stability and promote localized corrosion. This study investigates the effect of novel La Geria-inspired microstructures (LGMs) generated by laser surface texturing on the microstructure, microhardness, and electrochemical behavior of UNS S32750 super duplex stainless steel in 3.5 wt.% and 7.0 wt.% NaCl solutions, simulating seawater and concentrated desalination brine. Electrochemical results show that textured surfaces exhibit improved corrosion resistance, with more stable corrosion potentials, lower corrosion current densities, and higher impedance values. Microhardness measurements revealed a homogeneous mechanical response, confirming that laser texturing does not alter the mechanical integrity of the material. Microstructural observations showed reduced surface degradation and improved preservation of the duplex ferrite–austenite structure in textured samples after exposure to chloride solutions. These findings demonstrate that biomimetic laser surface texturing enhances corrosion resistance by modifying interfacial conditions and stabilizing the passive film, providing experimental evidence of the beneficial effect of LGMs in aggressive desalination environments.

Keywords: super duplex stainless steel; biomimetic surface texturing; corrosion resistance; electrochemical impedance spectroscopy; chloride environments; seawater desalination

Check for updates

Academic Editors: Kai Wang, Jingmang Xu and Yao Qian

Received: 2 July 2026
Revised: 24 July 2026
Accepted: 5 August 2026
Published: 11 August 2026

Copyright: © 2026 by the authors. Licensee MDPI, Basel, Switzerland. This article is an open access article distributed under the terms and conditions of the Creative Commons Attribution (CC BY) license.

1. Introduction

Limited freshwater availability has become a major concern in many arid and semi-arid regions around the world. As a consequence, seawater desalination has emerged as an essential technological solution for securing reliable drinking water supplies where conventional freshwater resources are insufficient [1–3]. Reverse osmosis is currently the most widely implemented desalination method due to its efficiency and scalability [4,5].

Natural seawater typically exhibits a salinity close to that represented by a 3.5 wt.% NaCl solution [6,7]. During desalination operations, dissolved salts accumulate in the concentrate stream, producing brines that may reach salinities close to 7.0 wt.% NaCl. These concentrated brines represent a service environment commonly encountered in reverse osmosis desalination plants and differ from natural seawater in terms of electrolyte composition, ionic strength, dissolved oxygen availability, and mass transport conditions. Consequently, they provide a representative environment for evaluating the electrochemical performance of structural materials used in desalination facilities rather than representing a universally more aggressive electrolyte. In addition, operating temperatures, typically in the range of 22–24 °C, may further promote electrochemical processes associated with metallic degradation [8].

Owing to their favorable balance between mechanical performance and corrosion resistance, duplex and super duplex stainless steels are among the preferred structural materials for desalination facilities operating in chloride-rich environments [9–12]. However, the specific electrochemical conditions associated with concentrated desalination brines and the need for enhanced durability have driven interest in improving their corrosion performance [13,14].

The excellent corrosion performance of super duplex stainless steels originates from their ferrite–austenite dual-phase microstructure together with elevated concentrations of chromium, molybdenum, and nitrogen, which provide enhanced resistance to localized corrosion, particularly in chloride-rich environments [15–17]. This duplex microstructure contributes to improved mechanical properties as well as increased resistance to pitting and stress corrosion cracking under high chloride concentrations [18,19]. The high resistance to localized corrosion of super duplex stainless steels is commonly associated with their elevated pitting resistance equivalent number (PREN), which depends primarily on the content of chromium, molybdenum, and nitrogen [16,20]. For super duplex grades, PREN values typically exceed 40, conferring excellent resistance to pitting corrosion in aggressive chloride environments [17].

Considerable research efforts have recently focused on surface engineering approaches aimed at enhancing the durability of metallic materials operating under chloride-rich service conditions [21–23]. Among these approaches, biomimetic surface design has attracted increasing attention due to its ability to modify interfacial phenomena such as electrolyte distribution and passive film stability [24,25].

Within this context, nature-inspired surface geometries represent an attractive strategy for modifying local electrolyte distribution and interfacial electrochemical conditions. Among them, the characteristic morphology of the vineyards of La Geria (Lanzarote, Canary Islands, Spain) provides an interesting example of a natural structure capable of influencing local flow patterns and mass transport processes. This effect is associated with changes in mass transport, flow dynamics, and passive film stability induced by controlled surface topographies. Figure 1 illustrates the typical operational environment of the present study.

Within this context, the morphology of the vineyards of La Geria represents an attractive example of a nature-inspired geometry capable of influencing local flow distribution and mass transport processes. Although originally developed as an agricultural adaptation to arid and windy volcanic environments, the characteristic crescent-shaped stone enclosures modify local wind patterns and create protected microenvironments around individual vines [26–28]. In surface engineering applications, the controlled generation of analogous crescent-shaped geometries through laser surface texturing may modify electrolyte distribution over metallic surfaces, reduce the formation of stagnant zones, and contribute to passive film stabilization [22,29–31].

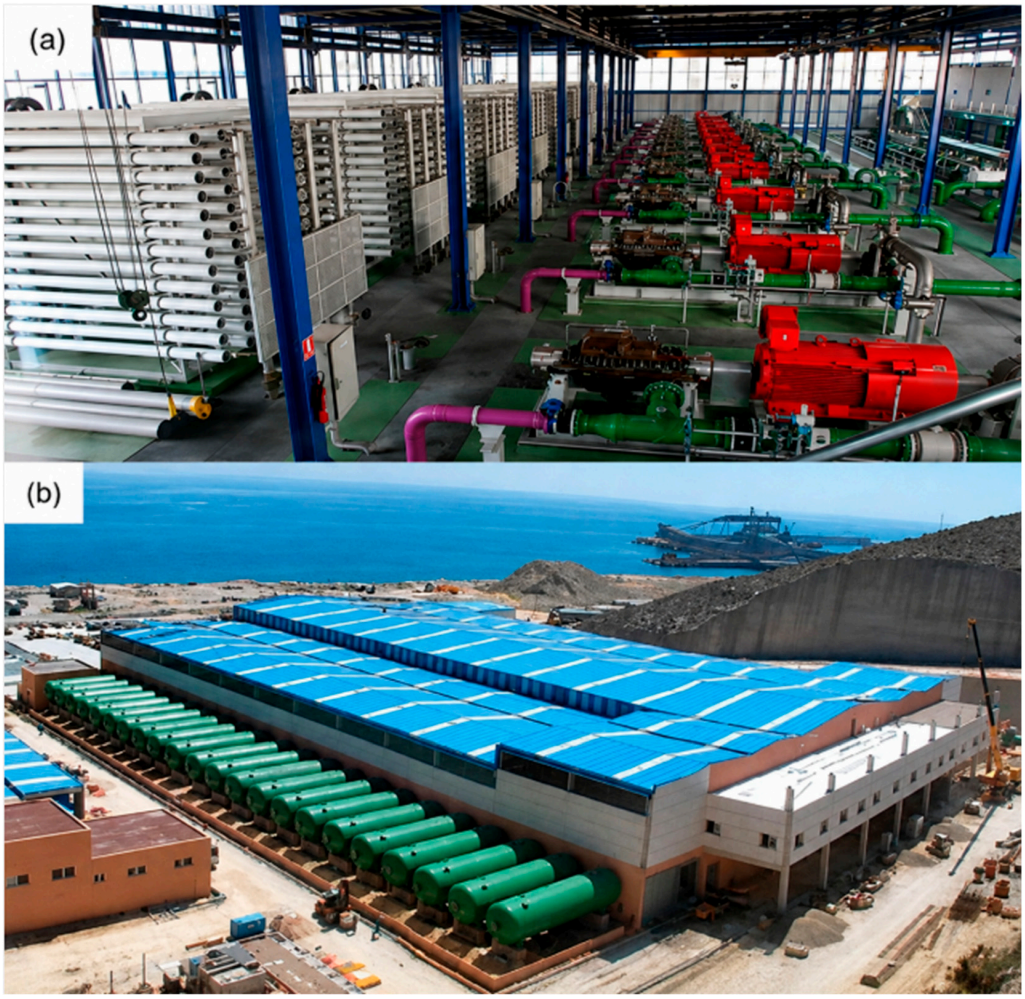


Figure 1. (**a**) Reverse osmosis desalination unit equipped with super duplex stainless steel components. (**b**) General view of the C9 desalination plant (Gran Canaria, Spain), representative of the operating conditions considered in this study.

Although super duplex stainless steels exhibit excellent intrinsic resistance to localized corrosion, their performance can be significantly affected under highly concentrated chloride conditions typical of desalination brines. While laser surface texturing has been explored as a strategy to improve corrosion resistance, the specific role of biomimetic surface geometries in modifying local electrochemical conditions remains unclear. In particular, there is a lack of systematic studies linking surface-induced hydrodynamic effects with passive film stability and dissolution kinetics under realistic desalination conditions [22,32,33].

In this context, the aim of the present study is to analyze the influence of biomimetic surface texturing inspired by La Geria vineyard morphology on the corrosion behavior of super duplex stainless steel in a chloride-rich environment. To this end, textured and non-textured surfaces are compared using electrochemical techniques in 3.5 wt.% and 7.0 wt.% NaCl solutions, simulating seawater and concentrated desalination brine, respectively.

The working hypothesis is that La Geria-inspired microstructures (LGMs) modify local electrolyte distribution, thereby enhancing passive film stability, increasing charge-transfer resistance, and reducing dissolution kinetics.

2. Materials and Methods

2.1. Material

The material used in this study was a commercially UNS S32750 grade super duplex stainless steel (Acerinox S.A., Los Barrios, Cádiz, Spain), widely employed in marine applications and seawater desalination infrastructures due to its high mechanical strength and excellent corrosion resistance in chloride-rich environments [10,15]. The chemical composition of the material was determined by X-ray fluorescence (XRF) using a handheld analyzer (Oxford Instruments X-MET7000 eXpress, Abingdon, UK) in order to verify its correspondence with the nominal composition of super duplex stainless steel.

Samples were sectioned from the base material using a precision cutting machine (Buehler IsoMet 4000, Chicago, IL, USA) under low-speed conditions with continuous water cooling to prevent thermal damage. The specimens were subsequently mounted in epoxy resin using a hot mounting press (Remet IPA 30 Evolution, Bologna, Italy) to facilitate handling and define the exposed working area.

Surface preparation was carried out using a Struers TegraPol-11 polishing machine (Copenhagen, Denmark). The samples were progressively ground using SiC abrasive papers with grit sizes of 320, 600, 800, 1200, and 2400, followed by mechanical polishing with diamond suspensions of 6 µm and 3 µm and a final polishing step using 1 µm alumina suspension to obtain a mirror-like surface finish. Between each preparation step, the samples were thoroughly rinsed with distilled water to remove debris.

Prior to electrochemical testing, the samples were rinsed with distilled water and allowed to air-dry under laboratory conditions. The exposed area of the working electrode was approximately 0.803 cm^2 for the non-textured sample and 0.810 cm^2 for the textured sample, as defined by the epoxy resin encapsulation. All surface preparation steps were carried out under controlled laboratory conditions to ensure reproducibility of the electrochemical measurements.

The detailed chemical composition of the investigated UNS S32750 alloy, determined by X-ray fluorescence (XRF), is presented in Section 3.1.

2.2. Surface Texturing

Biomimetic surface texturing was carried out using laser surface texturing (LST) technology with the aim of generating crescent-shaped microstructures inspired by the morphology of La Geria vineyard structures. This geometric pattern was designed to reproduce the characteristic shape of these natural structures, which are known for their ability to modify the interaction between solid surfaces and fluid flow [26–28].

In this study, two surface conditions were evaluated:

(a) Non-textured surface, used as the reference condition.
(b) Textured surface, characterized by a regular distribution of crescent-shaped microstructures generated by laser processing.

The texturing process was controlled to avoid significant alterations in the microstructure or mechanical properties of the base material.

Texturing Inspired by La Geria Vineyard Morphology

The design of the surface texturing pattern was inspired by the characteristic morphology of the vineyards of La Geria (Lanzarote, Canary Islands, Spain), a traditional agricultural system developed in volcanic environments and internationally recognized for its adaptation to arid and windy conditions [26–28]. As illustrated in Figure 2, this cultivation system consists of semicircular stone enclosures surrounding individual vines, creating a regular distribution of crescent-shaped structures across the terrain.

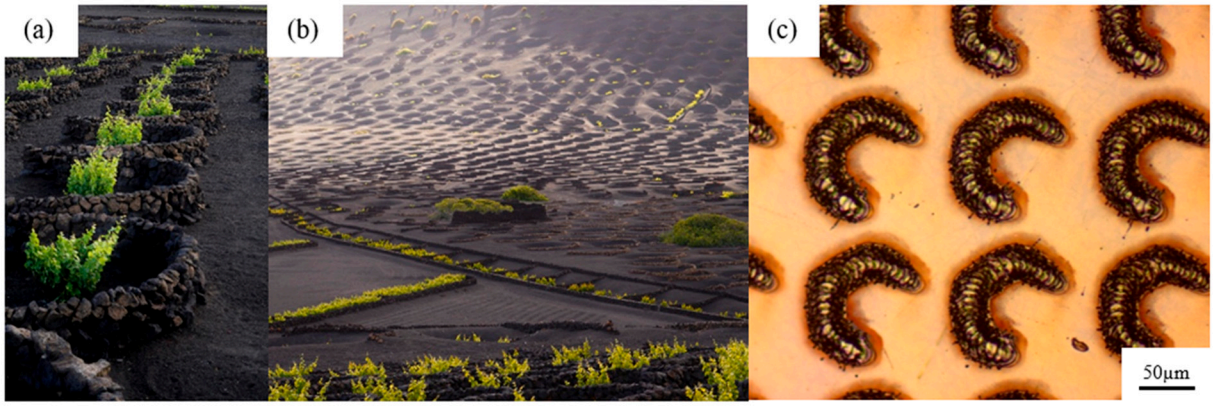


Figure 2. (**a**,**b**) Traditional cultivation structures characteristic of the La Geria region (Lanzarote, Spain), used as the natural inspiration for the biomimetic design. Images by the author. (**c**) Representative macroscopic photograph of the laser-textured UNS S32750 surface showing the periodic arrangement of the La Geria-inspired microstructures (LGMs) generated by laser surface texturing.

These structures were originally designed to protect vines from prevailing winds, improve moisture retention, and generate favorable local microenvironmental conditions in the volcanic soils of Lanzarote [26–28]. Their geometry modifies local flow patterns and influences the interaction between the protected central region and the surrounding environment. Consequently, they provide an attractive nature-inspired model for surface engineering applications, where local transport phenomena and fluid–surface interactions may significantly affect functional performance.

The laser-generated surface features investigated in this study are hereafter referred to as La Geria-inspired microstructures (LGMs). The present approach is considered biomimetic because it does not merely reproduce the visual appearance of the La Geria vineyard structures but rather translates their functional geometrical concept into an engineered metallic surface. Similar to the original agricultural structures, which modify local wind flow and create protected microenvironments around individual vines, the laser-generated crescent-shaped microstructures were designed to influence local electrolyte distribution and mass transport at the metal–electrolyte interface. Thus, the biomimetic concept adopted in this work is based on functional analogy rather than on direct geometric replication alone.

The replication of this type of morphology on metallic surfaces was proposed as a nature-inspired surface engineering strategy. The La Geria-inspired microstructures (LGMs) generated by laser surface texturing were designed to reproduce the characteristic crescent-shaped geometry of the vineyard enclosures, with the aim of modifying electrolyte distribution over the metallic surface and reducing the formation of stagnant fluid regions.

This type of surface geometry can influence the local hydrodynamics of the electrolyte and the distribution of electrochemically active species, such as chloride ions present in saline solutions. In particular, the presence of crescent-shaped structures may generate local flow gradients and promote electrolyte renewal processes at the metal–solution interface. As a result, La Geria-inspired microstructures may contribute to a more homogeneous electrolyte distribution and modify the stability of the passive film formed on the material surface [12,20,34].

In the present study, these microstructures were produced by laser surface texturing on super duplex stainless steel, resulting in a regular distribution of La Geria-inspired microstructures (LGMs). The objective of this surface modification was to evaluate its influence on the electrochemical behavior of the material in NaCl solutions representative of seawater (3.5 wt.%) and concentrated desalination brine (7.0 wt.%).

The nature-inspired surface texturing was carried out using a fiber laser system (Lansen LS30F, Qingdao, China) operating under laser ablation conditions. The process was performed with a scanning speed of 500 mm/s and a laser power of 15 W, generating microstructured features with a characteristic width of approximately 90 µm. This technique enables controlled material removal through localized thermal interaction, producing well-defined and reproducible surface geometries.

2.3. Microhardness Measurements

Vickers microhardness measurements were performed in accordance with ASTM E384-22 [35] using a microhardness tester (Future Tech FM-810, Kawasaki, Japan) to evaluate the mechanical behavior of the material. The tests were carried out using applied loads of 5, 25, 50, and 100 gf, with a dwell time of 15 s.

For each load condition, ten indentations were performed, and the average values along with the corresponding standard deviations were calculated. Statistical analysis of the results was carried out using one-way analysis of variance (ANOVA) to evaluate the effect of the applied load, followed by post hoc multiple comparisons using the Bonferroni correction method.

2.4. Electrochemical Testing

Electrochemical measurements were carried out using a conventional three-electrode electrochemical cell connected to a potentiostat (Bio-Logic SP-150, Seyssinet-Pariset, France). The sample served as the working electrode, while a platinum electrode and a saturated calomel electrode (SCE) were used as the counter and reference electrodes, respectively, following ISO 10271:2020 [36]. The tests were carried out in aqueous sodium chloride solutions with concentrations of 3.5 wt.% and 7.0 wt.%, simulating seawater and concentrated desalination brine, respectively.

For OCP measurements, the "E_{corr} vs. Time" method in EC-Lab software V. 9.55 was applied over 24 h. Potentials were recorded at 120 s intervals or upon changes exceeding 100 mV until stabilization was achieved. Results are presented as potential-time curves.

A linear polarization test was conducted with a scan rate of 0.166 mV/s within a potential range of ±25 mV relative to OCP, and data were recorded every 0.5 s. Then, generalized corrosion analysis was carried out over a potential range from −0.7 V vs. SCE to +0.5 V vs. OCP at a scan rate of 10 $mV \cdot min^{-1}$. The corrosion current density (i_{corr}) was determined by Tafel extrapolation ("Tafel fit") and the corresponding corrosion rate was calculated according to ASTM G102-23 [37]). Additionally, the polarization resistance (R_{pol}) was calculated using the "Rp fit" method.

Finally, electrochemical impedance spectroscopy (EIS) measurements were carried out over the frequency range from 200 kHz to 100 mHz using a 0 V perturbation relative to the open-circuit potential (OCP). The measurements followed the procedures outlined in ISO 16773-1:2016 [38] and the resulting impedance spectra are presented as Nyquist and Bode plots. Equivalent circuit (EC) models were employed to fit the experimental spectra.

Experimental data were fitted using ZSimpWin V.3.60 software with an equivalent circuit. The quality of the fitting was evaluated using the chi-square (χ^2) parameter.

All electrochemical measurements were carried out under controlled laboratory conditions at 22 ± 2 °C to ensure stable experimental conditions and reproducibility of the results.

2.5. Surface Characterization

After electrochemical testing, the sample surfaces were examined using an optical microscope (Axio Vert.A1 MAT ZEISS, Jena, Germany) under different conditions, namely before electrochemical testing, after exposure to a 3.5 wt.% NaCl solution, after exposure to a 7.0 wt.% NaCl solution, and after chemical etching with V2A reagent, in order to

identify possible corrosion attack mechanisms, evaluate microstructural changes induced by exposure to a saline environment, and reveal the microstructure of the samples. The V2A reagent consisted of a solution containing 100 mL of hydrochloric acid (HCl), 100 mL of nitric acid (HNO_3), and 100 mL of distilled water, commonly used for metallographic etching of austenitic and duplex stainless steels.

The chemical etching was performed at 60 °C for 1.5 min, after which the samples were immediately rinsed with distilled water to stop the etching reaction, then cleaned with alcohol, and finally air-dried under laboratory conditions.

3. Results and Discussion

The results presented in this section were obtained from the Supplementary Materials section.

3.1. Chemical Composition

The XRF characterization confirmed that the studied material corresponds to a super duplex stainless steel of UNS S32750 grade. As shown in Figure 3, the alloy exhibits high Cr and Mo contents, which are key elements for the formation and stability of the protective passive film in chloride-rich environments.

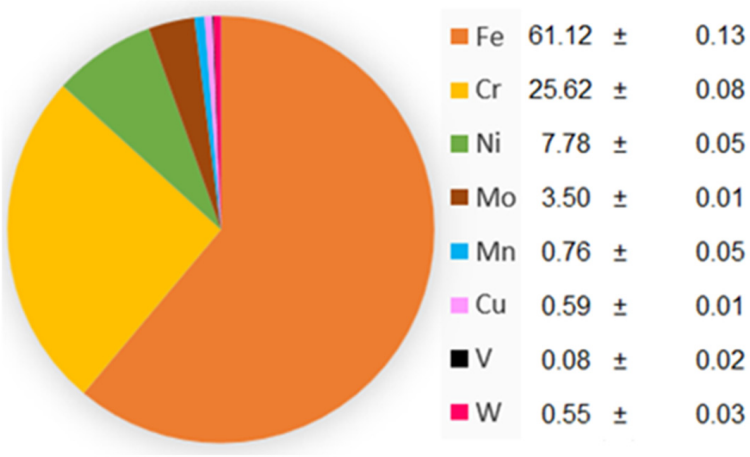


Figure 3. Chemical composition (in wt.%) of the UNS S32750 super duplex stainless steel determined by XRF.

These alloying elements play a critical role in enhancing resistance to localized corrosion, particularly pitting corrosion and stress corrosion cracking, under high chloride concentrations. The presence of Mo is especially relevant for improving pitting resistance, while Cr contributes to the formation of a stable and protective passive oxide layer.

3.2. Microhardness

The Vickers microhardness values obtained under different applied loads are presented in Figure 4. The results show a load-dependent hardness response, with moderate variations among the different applied loads. Although the average hardness values vary significantly with indentation load, they remain within the characteristic hardness range reported for UNS S32750 super duplex stainless steel, indicating that the laser surface texturing process did not produce substantial changes in the intrinsic mechanical properties of the material.

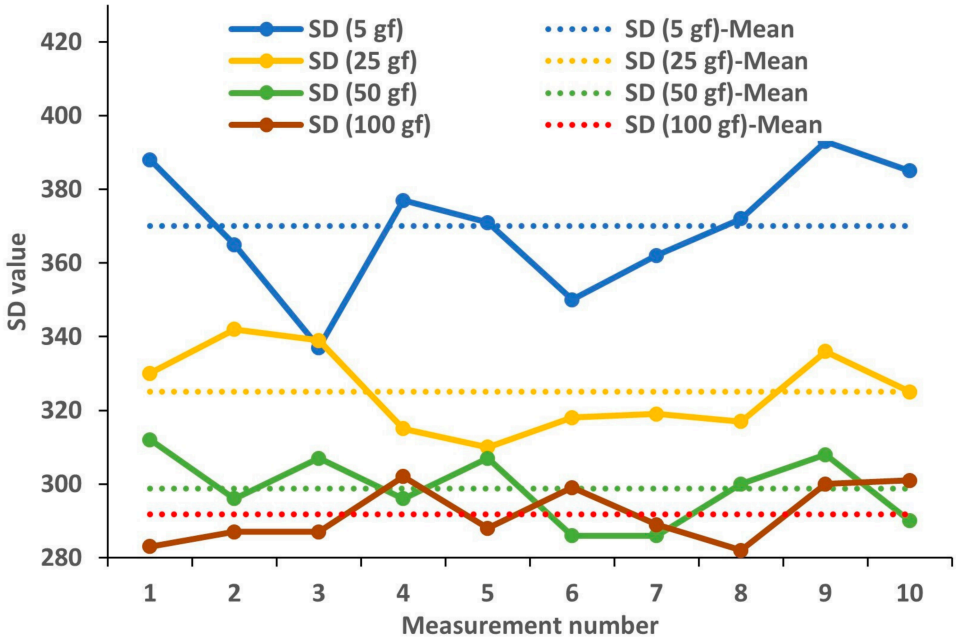


Figure 4. Vickers microhardness values obtained at different applied loads (5, 25, 50 and 100 gf) of the super duplex (SD) material.

In order to evaluate the effect of the applied load on the measured values, a one-way analysis of variance (ANOVA) was performed. The results confirmed a statistically significant effect of the applied load on microhardness values ($F(3.36) = 87.16$, $p < 0.001$). Although statistically significant differences were detected between the mean hardness values, their absolute magnitude remained relatively small, and all measurements fell within the expected hardness range for super duplex stainless steel. Therefore, the observed variations should be interpreted as load-dependent rather than as evidence of changes in the intrinsic mechanical behavior of the material, as shown in Table 1.

Table 1. One-way ANOVA results evaluating the effect of applied load on Vickers microhardness measurements.

Source	SS	df	MS	F	*p*-Value
Between groups	37,625.67	3.00	12,541.89	87.16	<0.001
Within groups	5180.10	36.00	143.89		
Total	42,805.77	39.00			

Note. SS = sum of squares; df = degrees of freedom; MS = mean square; F = Fisher's F-statistic; *p*-value = probability associated with the F-test.

Multiple comparisons using Bonferroni correction (see Table 2) revealed significant differences between most load conditions. However, no statistically significant differences were observed between 50 gf and 100 gf ($p = 0.089$), suggesting that the influence of the indentation size effect (ISE) decreases at higher loads.

Overall, these results indicate that increasing the applied load reduces the influence of the indentation size effect, while the measured hardness values remain within the characteristic range of the alloy. These results suggest that the laser surface texturing process did not produce significant alterations in the mechanical properties or in the microstructural integrity of the material.

This behavior is primarily associated with the well-known indentation size effect (ISE), a common phenomenon in microhardness testing at low loads. However, local microstructural heterogeneity related to the ferrite–austenite phase distribution, together

with the random position of the indentation relative to the two phases, may also contribute to the measured hardness variability [12,39].

Table 2. Pairwise comparisons using Bonferroni correction.

Comparison	*p*-Value	Result
5 gf vs. 25 gf	4.59×10^{-6}	Significant
5 gf vs. 50 gf	1.90×10^{-8}	Significant
5 gf vs. 100 gf	1.25×10^{-8}	Significant
25 gf vs. 50 gf	2.31×10^{-5}	Significant
25 gf vs. 100 gf	7.56×10^{-7}	Significant
50 gf vs. 100 gf	8.97×10^{-2}	Not significant

Furthermore, despite the load-dependent variations observed, the hardness values remained within the expected range for UNS S32750 super duplex stainless steel, indicating that the laser surface texturing process did not generate heat-affected zones capable of significantly modifying the intrinsic mechanical properties of the material. This observation is particularly relevant because it indicates that the differences observed in corrosion behavior are primarily associated with surface topography modification rather than with changes in the intrinsic mechanical properties of the base material.

It should also be noted that the present microhardness measurements do not provide direct evidence that laser surface texturing modified the intrinsic mechanical properties of the substrate. The observed hardness variability is primarily associated with the indentation size effect and local microstructural heterogeneity, whereas the measured hardness values remain within the characteristic range reported for UNS S32750 super duplex stainless steel. Consequently, the present results do not support the existence of significant laser-induced mechanical degradation under the selected processing conditions.

The ANOVA results revealed a statistically significant effect of the applied load on Vickers microhardness measurements ($F = 87.16$, $p < 0.001$), indicating that the measured hardness values varied significantly with indentation load.

3.3. Electrochemical Testing

An estimation of the alloy susceptibility to localized corrosion was obtained through the pitting resistance equivalent number (PREN). The calculated value, close to 41 (Table 3), places the investigated material within the range commonly associated with super duplex stainless steels. Such a value reflects the combined contribution of chromium, molybdenum, and nitrogen to passive film stability and provides a useful reference for interpreting the electrochemical response obtained in chloride-containing media.

Table 3. Calculation of the pitting resistance equivalent number (PREN) based on the chemical composition of the UNS S32750 super duplex stainless steel.

Element	Content (wt.%)	PREN Factor	Contribution
Cr	25.62	1.0	25.62
Mo	3.33	3.5	10.99
N	0.27	16.0	4.32
Total			40.93

Note. The N content was estimated based on typical values reported in the literature for UNS S32750 super duplex stainless steel, as N cannot be reliably determined by X-ray fluorescence analysis.

The high chromium content promotes the formation of a chromium-rich passive oxide layer that protects the material against general corrosion. In turn, molybdenum

enhances resistance to localized corrosion, particularly in environments with high chloride concentrations. In addition, the presence of nitrogen in super duplex stainless steels significantly contributes to improving resistance to localized corrosion under aggressive chloride conditions. These characteristics make super duplex stainless steels widely used in marine applications and seawater desalination facilities [40].

The obtained chemical composition is consistent with that of typical super duplex stainless steels used in structural components exposed to highly aggressive environments, such as pipelines, pumps, and fluid transport systems in desalination plants. Based on the chemical composition determined by XRF, the theoretical density of the alloy was estimated using the rule of mixtures, considering the densities of the constituent elements. The calculated value was approximately 7.92 $g \cdot cm^{-3}$, which agrees with typical values reported for UNS S32750 super duplex stainless steels, generally ranging between 7.8 and 8.0 $g \cdot cm^{-3}$.

The pitting resistance equivalent number (*PREN*) was calculated from the chemical composition using the following expression:

$$PREN = \%Cr + 3.3 \times \%Mo + 16 \times \%N \quad (1)$$

The obtained *PREN* value (40.93), approximately 41, confirms the high resistance of the material to localized corrosion in chloride-rich environments, as expected for super duplex stainless steels. The obtained PREN value is consistent with the high corrosion resistance generally reported for UNS S32750 super duplex stainless steels exposed to chloride-containing environments. The relationship between alloy chemistry and the electrochemical behavior observed in the present work is discussed in the following sections.

3.3.1. Evolution of the Open-Circuit Potential (OCP)

As seen in Figure 5, the evolution of the corrosion potential of each sample was monitored over 24 h in 3.5% and 7.0% NaCl solutions. In this case, the electrochemical stability of the surface during exposure is shown by the temporal fluctuation of E_{corr}.

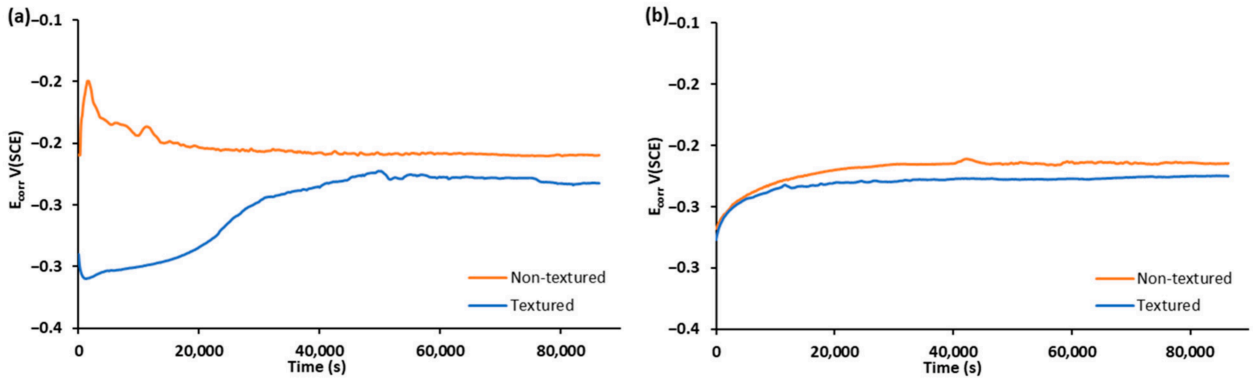


Figure 5. Evolution of the OCP over 24 h of immersion for textured and non-textured super duplex stainless steel surfaces in NaCl solutions: (**a**) 3.5 wt.% and (**b**) 7.0 wt.%.

The non-textured and textured samples' corrosion potential varied depending on the environments. During the first three hours of immersion at 3.5% NaCl, the E_{corr} of the non-textured sample increases rapidly and then shows a gradual decrease over time, whereas the textured sample shifts towards less negative values. This behavior continues throughout the rest of the test.

However, both samples exhibited similar responses during the 24 h immersion period in a 7.0% NaCl solution, as their E_{corr} tended to increase until it stabilized.

In both electrolytes, the textured surfaces exhibited a comparatively stable OCP evolution. However, the final potential values depended on NaCl concentration. In 3.5 wt.% NaCl, the textured condition showed a slightly more negative corrosion potential than the non-textured condition, whereas in 7.0 wt.% NaCl, the textured condition exhibited a more positive potential. These relatively small potential shifts indicate that laser texturing modifies the balance between the anodic and cathodic interfacial reactions. Nevertheless, the corrosion potential alone does not provide a direct measure of the corrosion rate and must be interpreted together with the corrosion current density and polarization resistance.

3.3.2. Polarization and Potentiodynamic Curves

The linear polarization curves obtained for both surface conditions in the two NaCl solutions are presented in Figure 6, and the corresponding polarization resistance values are summarized in Table 4. Laser texturing produced relatively small shifts in the electrochemical potential but more evident changes in polarization resistance. In 3.5 wt.% NaCl, the textured surface exhibited a slightly more negative corrosion potential than the non-textured surface. This shift does not necessarily indicate a higher corrosion rate, because the corrosion potential represents the mixed potential established by the balance between anodic metal dissolution and cathodic reactions. Therefore, its interpretation must be supported by kinetic parameters such as corrosion current density and polarization resistance.

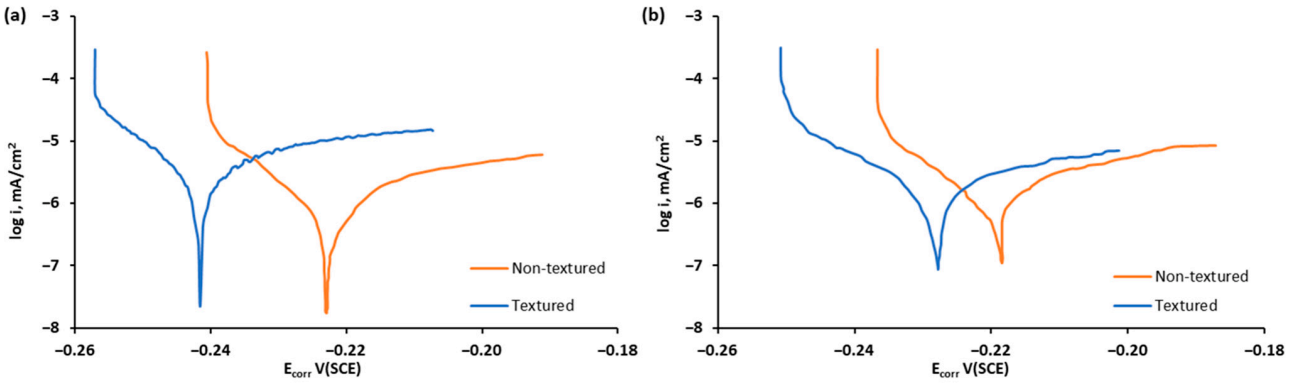


Figure 6. Linear polarization curves obtained for textured and non-textured super duplex stainless steel surfaces in NaCl solutions: (**a**) 3.5 wt.% and (**b**) 7.0 wt.%.

Table 4. Polarization resistance values obtained from linear polarization measurements for non-textured and laser-textured UNS S32750 super duplex stainless steel surfaces exposed to 3.5 wt.% and 7.0 wt.% NaCl solutions.

Surface Condition	NaCl (wt.%)	Polarization Resistance, R_{pol} ($\Omega \cdot cm^2$)
Non-textured	3.5	5.20×10^6
Textured	3.5	2.53×10^6
Non-textured	7.0	3.60×10^6
Textured	7.0	3.30×10^6

The lower corrosion current density subsequently obtained for the textured surface in 3.5 wt.% NaCl indicates that, despite the slightly more negative corrosion potential, the overall corrosion kinetics were reduced. The potential displacement may be associated with laser-induced changes in surface condition, active area, roughness, and the relative kinetics of the anodic and cathodic reactions at the metal–electrolyte interface.

The linear polarization results show that the textured surface exhibited lower R_{pol} values than the non-textured surface, particularly in 3.5 wt.% NaCl. Therefore, the effect of

texturing was not uniformly beneficial for all electrochemical indicators, and the decrease in i_{corr} obtained by Tafel analysis should be interpreted together with the independently measured polarization resistance.

The potentiodynamic curves obtained for both surface conditions are presented in Figure 7. The curves exhibit a typical passivation behavior characteristic of stainless steels in chloride-containing environments. In both cases, a relatively stable passive region is observed. Nevertheless, the textured surfaces show slightly lower anodic currents, indicating enhanced electrochemical stability. The electrochemical parameters derived from the potentiodynamic polarization curves are summarized in Table 5. In general, the textured surfaces exhibited slightly lower corrosion current density (i_{corr}) values than the non-textured surfaces, suggesting a tendency toward reduced corrosion kinetics. This tendency was more evident in the 3.5 wt.% NaCl solution, representative of natural seawater. However, the differences in E_{corr}, i_{corr}, and Tafel slopes were relatively moderate, indicating that the polarization curves alone do not provide conclusive evidence of the effect of laser surface texturing. Therefore, these results should be interpreted together with the complementary electrochemical analyses, particularly the EIS measurements, which provide additional information on passive film stability and charge-transfer processes.

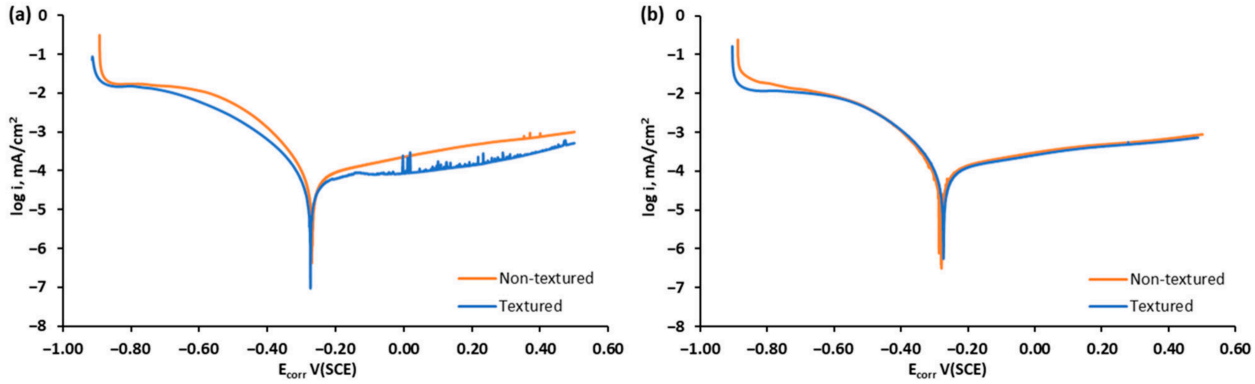


Figure 7. Potentiodynamic curves obtained for textured and non-textured super duplex stainless steel surfaces in NaCl solutions: (**a**) 3.5 wt.% and (**b**) 7.0 wt.%.

Table 5. Electrochemical parameters derived from polarization curves for textured and non-textured super duplex stainless steel surfaces in NaCl solutions.

Surface Condition	NaCl (wt.%)	E_{corr} (mV vs. SCE)	i_{corr} (μA/cm^2)	β_c (mV)	β_a (mV)	CR (mm·year^{-1})	R_{pol} (Ω)
Non-textured	3.50	−269.49	0.039	82.7	272.0	4.83×10^{-4}	5.2×10^{6}
Textured	3.50	−273.66	0.016	62.0	120.3	1.96×10^{-4}	2.53×10^{6}
Non-textured	7.00	−280.91	0.058	99.4	304.8	7.19×10^{-4}	3.6×10^{6}
Textured	7.00	−273.25	0.056	94.8	303.3	6.88×10^{-4}	3.3×10^{6}

The equivalent weight of each sample to calculate the corrosion rate (CR) was estimated according to ASTM G102-23 using the following expression:

$$W = \frac{1}{\sum (n_i \cdot f_i / W_i)} \quad (2)$$

where f_i represents the mass fraction, W_i is the atomic weight, and n_i is the assumed valence of each element. By considering the principal alloying elements with contents greater than 1 wt.%, an equivalent weight of 24.1 g·equiv^{-1} was obtained.

The electrochemical parameters obtained from Tafel extrapolation are fully consistent with the trends observed in the polarization curves. For the 3.5 wt.% NaCl solution, laser texturing reduced the corrosion rate from 4.83×10^{-4} to 1.96×10^{-4} mm·year^{-1}. Under the 7.0 wt.% NaCl condition, the reduction was less pronounced, decreasing from 7.19×10^{-4} to 6.88×10^{-4} mm·year^{-1}. In all cases, the measured corrosion rates remained within the 10^{-4} mm·year^{-1} range, confirming the outstanding corrosion resistance of UNS S32750 super duplex stainless steel. Previous studies on 18Mn-18Cr austenitic stainless steel in 3.5 wt.% NaCl reported corrosion current densities of approximately 0.06 μA·cm^{-2} at 25 °C, increasing significantly with temperature, whereas the present textured super duplex sample showed a lower i_{corr} value of 0.016 μA·cm^{-2} under comparable room-temperature chloride conditions. Recent work on 304 and S31254 stainless steels in 3.5 wt.% NaCl also demonstrated that higher-alloyed stainless steels exhibit lower corrosion currents and improved passive film stability than conventional 304 stainless steel, supporting the trend observed here for the super duplex alloy [23]. Overall, these comparisons indicate that the corrosion performance obtained in the present work is consistent with the high PREN value of the investigated alloy. The results further suggest that the biomimetic laser-textured surface contributes to maintaining passive film stability under chloride-rich conditions.

This difference can be attributed to the changes in electrolyte composition associated with the concentrated NaCl solution, which may influence passive film stability, dissolved oxygen availability, and interfacial electrochemical conditions. Under these conditions, the beneficial effect of surface texturing is partially limited, although the textured surfaces consistently exhibited improved corrosion resistance, indicating that the biomimetic geometry continues to promote a more uniform electrolyte distribution and to mitigate localized electrochemical activity.

Changes in the electrochemical reaction are also reflected in Tafel slopes. The textured sample exhibits lower anodic and cathodic slopes (β_a and β_c, respectively) at 3.5 and 7.0% NaCl than the non-textured sample, indicating that the anodic and cathodic branches of the potentiodynamic curves behave differently.

These results suggest that the effectiveness of the biomimetic surface is dependent on the severity of the corrosive environment, remaining significant under moderate conditions and still beneficial, although reduced, under highly aggressive chloride concentrations.

The differences observed in the polarization curves were relatively moderate, particularly with respect to the corrosion potential and Tafel slopes. Therefore, the corrosion behavior was not interpreted exclusively from the polarization measurements. Electrochemical impedance spectroscopy (EIS) was employed as a complementary technique to further evaluate the passive film characteristics and charge-transfer processes. The EIS results, discussed in the following section, confirmed the improved electrochemical performance of the textured surfaces by showing higher impedance values and increased charge-transfer resistance. Consequently, the conclusions of the present study are based on the combined interpretation of OCP, linear polarization, potentiodynamic polarization, and EIS measurements.

3.3.3. Electrochemical Impedance Spectroscopy (EIS)

The electrochemical impedance spectra are presented in Figures 8 and 9 in the form of Nyquist and Bode plots, respectively.

Compared with the non-textured condition, the laser-textured surfaces exhibited slightly larger capacitive loops and moderately higher impedance responses in the Nyquist representation. The differences were more evident in the 3.5 wt.% NaCl solution, whereas both surface conditions displayed very similar responses in the 7.0 wt.% NaCl solution.

These observations indicate that the influence of laser surface texturing on the global electrochemical response was moderate and depended on the electrolyte composition.

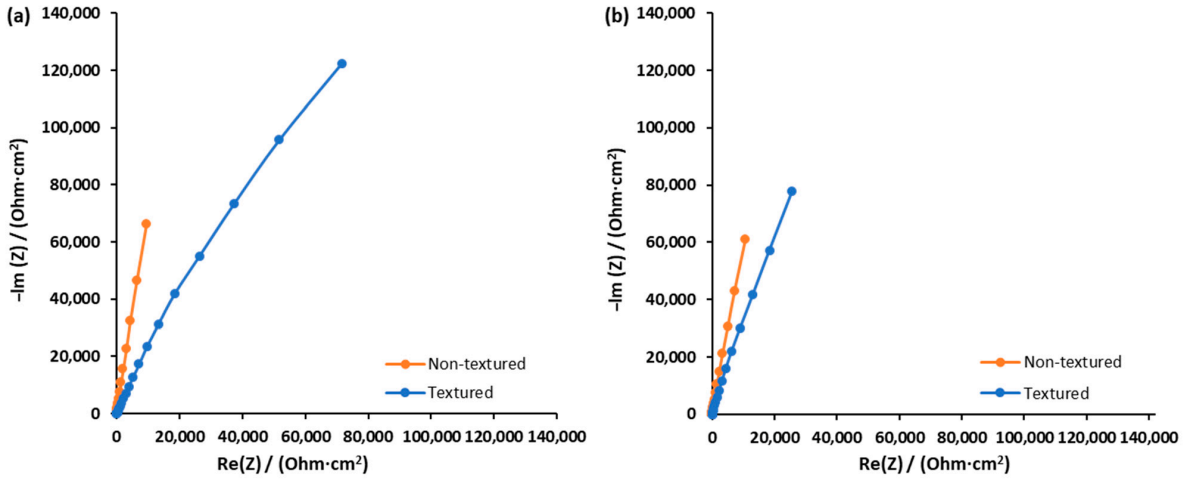


Figure 8. Nyquist plots obtained by EIS for textured and non-textured super duplex stainless steel surfaces in NaCl solutions: (**a**) 3.5 wt.% and (**b**) 7.0 wt.%.

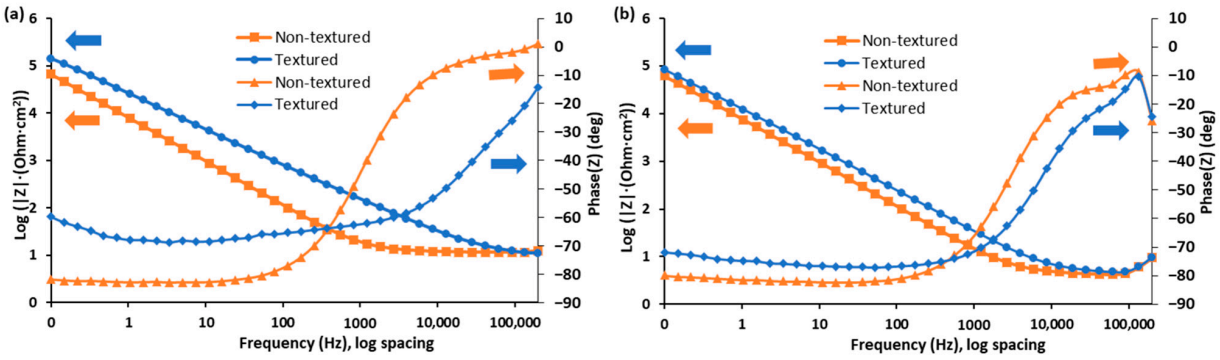


Figure 9. Bode plots obtained by EIS for textured and non-textured super duplex stainless steel surfaces in NaCl solutions: (**a**) 3.5 wt.% and (**b**) 7.0 wt.%.

Although the qualitative differences observed in the Nyquist plots were relatively small, particularly under the 7.0 wt.% NaCl condition, the impedance spectra remained consistent with the equivalent-circuit fitting results, which showed slightly higher charge-transfer resistance values for the textured surfaces. Consequently, the electrochemical behavior was interpreted considering both the experimental spectra and the quantitative fitting parameters rather than the graphical appearance of the Nyquist plots alone.

Furthermore, Bode diagrams are represented by the impedance modulus (|Z|) and phase angle as a function of frequency.

From high frequencies to low frequencies, it can be seen that under both conditions (3.5% and 7.0% NaCl solutions), the behavior of the curves showing absolute impedance values is similar, with maximum impedance values for the textured sample. However, the maximum phase angles were obtained by the non-textured sample (approximately 85°), while the textured sample obtained values between 70 and 75° in both solutions.

The Bode plots showed only modest differences between textured and non-textured surfaces. The increase in low-frequency impedance was more noticeable in the 3.5 wt.% NaCl solution, whereas both surface conditions exhibited very similar impedance modulus and phase-angle responses in the 7.0 wt.% NaCl solution. Therefore, the qualitative Bode plots alone do not provide conclusive evidence of the effect of laser surface texturing and should be interpreted together with the equivalent-circuit fitting parameters.

After the corrosion test, both Nyquist and Bode plots show a general decrease in impedance values, indicating a certain degradation of the passive film due to exposure to the corrosive environment. Nevertheless, the textured surfaces maintain higher impedance values compared to the non-textured surfaces, suggesting enhanced electrochemical stability even after exposure to highly concentrated chloride solutions.

The electrochemical behavior of the samples was fitted using an electrical equivalent circuit of the R(QR) type. The use of a constant phase element (CPE) instead of an ideal capacitor accounts for surface heterogeneity and interfacial roughness at the metal–electrolyte interface, particularly in textured surfaces, leading to deviations from ideal capacitive behavior [41].

In this model, R_1 represents the solution resistance, Q_2 corresponds to the CPE associated with the non-ideal capacitive behavior of the metal–electrolyte interface, and R_2 represents the charge-transfer resistance related to the corrosion process (see Figure 10). Since the corrosion current density is inversely proportional to the charge-transfer resistance, the increase in R_2 observed for the textured surfaces confirms a reduction in corrosion kinetics and an overall improvement in the electrochemical performance of the material.

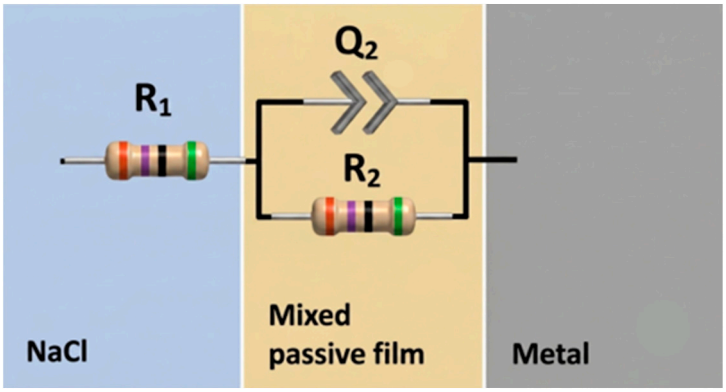


Figure 10. R(QR) equivalent circuit used to fit the electrochemical impedance spectra.

The electrochemical parameters obtained from fitting the R(QR) equivalent circuit are presented in Table 6. The textured surfaces exhibit higher resistance values associated with the passive film, indicating improved electrochemical stability and enhanced resistance to corrosive attack. These results are consistent with the Nyquist and Bode plots, as well as with the reduction in corrosion current density observed in the polarization measurements.

Table 6. Electrochemical parameters obtained from fitting the R(QR) equivalent circuit for textured and non-textured super duplex stainless steel surfaces in NaCl solutions. Charge-transfer resistance (R_2), constant phase element parameters (Q_2, n_2), and fitting quality parameter (χ^2) are included.

Surface Condition	NaCl (wt.%)	R_2 ($\Omega \cdot cm^2$)	Q_2 ($S \cdot sn \cdot cm^{-2}$)	CPE Exponent (n_2)	χ^2
Non-textured	3.50	2.09×10^6	2.26×10^{-5}	0.92	2.42×10^{-4}
Textured	3.50	2.22×10^6	9.88×10^{-6}	0.74	1.67×10^{-3}
Non-textured	7.00	8.69×10^5	2.37×10^{-5}	0.91	7.96×10^{-3}
Textured	7.00	9.01×10^5	1.65×10^{-5}	0.85	6.07×10^{-3}

This behavior agrees with polarization results, where the textured surfaces showed lower corrosion current densities. Since corrosion current density is inversely related to charge-transfer resistance, the increase in R_2 further confirms the improved corrosion resistance of the textured surfaces.

In the 3.5 wt.% NaCl solution, the textured surface exhibited an increase of approximately 6% in charge-transfer resistance (R_2) compared to the non-textured surface. In 7.0 wt.% NaCl, the increase was approximately 4%, indicating a moderate improvement in corrosion resistance associated with surface texturing.

Overall, the results obtained from OCP, polarization measurements, and electrochemical impedance spectroscopy indicate that biomimetic surface texturing modifies the surface topography and produces a moderate improvement in the electrochemical response of the material. The effect was more evident in the 3.5 wt.% NaCl solution, whereas smaller differences were observed in the 7.0 wt.% NaCl solution.

The crescent-shaped La Geria-inspired microstructures (LGMs) may promote a more homogeneous electrolyte distribution over the metallic surface and reduce the formation of stagnant regions. Consequently, the electrochemical response is consistent with a modest improvement in passive film performance and a reduced tendency for localized corrosion initiation. However, this interpretation is based on the combined analysis of the electrochemical measurements and the equivalent-circuit fitting results rather than on any individual electrochemical technique alone.

The PREN value (~41), characteristic of super duplex stainless steels, is consistent with the high corrosion resistance observed experimentally, reflected in low corrosion current densities and high charge-transfer resistance (R_2). In this context, the results indicate that, while chemical composition governs the intrinsic resistance of the material to localized corrosion, biomimetic surface texturing provides an additional contribution by optimizing the electrochemical conditions at the metal–electrolyte interface.

This behavior highlights a synergistic effect between alloy composition and surface modification in enhancing corrosion resistance in chloride-rich environments. While the high alloying content governs the intrinsic resistance of the material to localized corrosion, the biomimetic surface texturing modifies the local electrochemical environment at the metal–electrolyte interface. In particular, the textured geometry promotes a more uniform electrolyte distribution and reduces localized accumulation of aggressive species, thereby contributing to improved passive film stability. Consequently, the observed improvement cannot be attributed solely to geometric factors but also to the electrochemical stabilization of the passive layer induced by modified interfacial conditions.

3.4. Surface Analysis

The microstructural analysis performed by optical microscopy is presented in Figure 11. Observations carried out before and after electrochemical testing reveal clear differences between textured and non-textured surfaces.

The optical micrographs reveal differences in surface condition after exposure to the two NaCl concentrations, although no substantial modification of the underlying ferrite–austenite morphology was detected at the resolution of the optical microscopy technique. The non-textured surfaces exposed to 3.5 wt.% NaCl showed dispersed darkened regions and localized surface features that may be associated with preferential electrochemical activity. After exposure to 7.0 wt.% NaCl, a greater number of surface irregularities and polishing marks were visible, indicating a stronger influence of the concentrated chloride environment on the surface condition. Nevertheless, the characteristic duplex microstructure remained identifiable after chemical etching.

The ferrite and austenite phases of UNS S32750 may exhibit different electrochemical responses because of their different Cr, Mo, Ni, and N contents. Previous studies have reported that localized corrosion in duplex stainless steels may preferentially initiate at phase boundaries or in regions where local elemental partitioning produces differences in passive film stability [22,39,40]. In particular, increasing chloride concentration facilitates

competitive adsorption of chloride ions on the passive surface and may promote local passive film breakdown, although the high Cr, Mo, and N contents of UNS S32750 provide strong resistance to these processes.

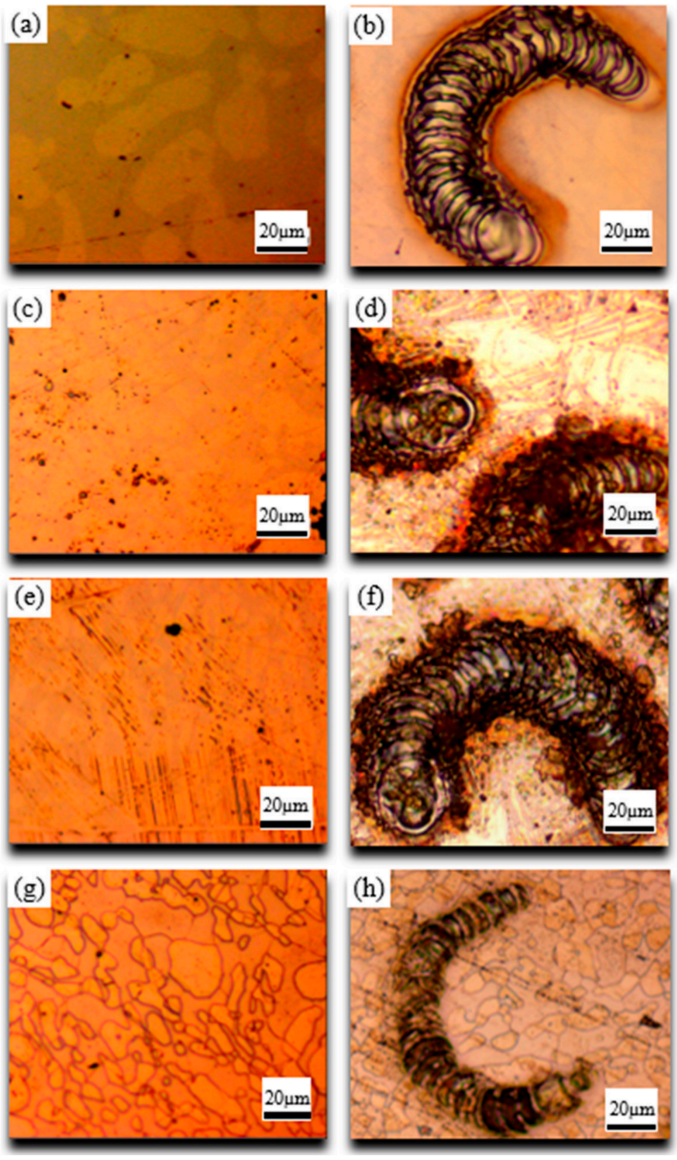


Figure 11. Optical microscopy images of non-textured and textured super duplex stainless steel surfaces under different conditions: before corrosion testing (**a**,**b**), after exposure to 3.5 wt.% NaCl solution (**c**,**d**), after exposure to 7.0 wt.% NaCl solution (**e**,**f**) and after chemical etching with V2A reagent to reveal the microstructure (**g**,**h**).

In the present study, the differences between the 3.5 wt.% and 7.0 wt.% NaCl conditions were mainly observed as changes in surface degradation rather than as transformations of the ferrite–austenite microstructure. This is consistent with the relatively short exposure time and the absence of thermal or mechanical conditions capable of inducing phase transformation. The textured surfaces showed a more localized distribution of surface alteration around the laser-generated features, while the surrounding regions remained comparatively preserved. However, because the observations were obtained by optical microscopy, they should be interpreted as qualitative evidence of differences in surface condition rather than as direct proof of changes in phase composition or passive-film chemistry.

These observations are broadly consistent with previous studies showing that the corrosion response of duplex and super duplex stainless steels in chloride-containing

media is governed by the interaction between phase distribution, local alloy chemistry, and passive film stability [20,22,39,40]. The optical microscopy results therefore complement the electrochemical measurements by showing that the increase from 3.5 wt.% to 7.0 wt.% NaCl affects the extent and distribution of surface alteration, while the underlying duplex microstructure remains preserved.

The images highlight the differences in surface degradation and microstructural preservation between the two surface conditions.

4. Conclusions

This study demonstrates that biomimetic laser surface texturing significantly improves the corrosion resistance of super duplex stainless steel in chloride-rich environments representative of seawater and desalination brine. Based on the obtained results, the following conclusions can be drawn:

(a) Chemical composition analysis confirmed that the material corresponds to UNS S32750 super duplex stainless steel, characterized by high chromium and molybdenum contents that promote the formation of a stable passive film in chloride-rich environments.

(b) Vickers microhardness tests revealed a homogeneous mechanical response, indicating that the laser surface texturing process did not induce significant changes in the mechanical properties or microstructure of the base material.

(c) Open-circuit potential measurements showed progressive stabilization associated with passive film formation, with textured surfaces exhibiting more stable electrochemical behavior. Polarization and potentiodynamic curves and derived electrochemical parameters indicated lower corrosion current densities for the textured surfaces compared to the non-textured ones, confirming a reduction in corrosion rate under high-chloride conditions. Electrochemical impedance spectroscopy and equivalent circuit fitting revealed higher impedance values and increased charge-transfer resistance (R_2) for the textured surfaces, indicating enhanced electrochemical stability.

Microstructural analysis confirmed reduced surface degradation in textured samples after exposure to the corrosive environment, suggesting that the La Geria-inspired microstructures (LGMs) promote a more uniform electrolyte distribution and improve passive film stability.

Taken together, the experimental findings indicate that corrosion performance results from the combined contribution of alloy chemistry and biomimetic surface architecture, highlighting laser-induced surface texturing as an effective strategy to enhance the durability of super duplex stainless steels in highly aggressive desalination environments. This approach could be extended to other corrosion-resistant alloys exposed to aggressive marine environments.

Future work will include SEM/EDS characterization of the laser-textured regions to evaluate possible local compositional modifications, including chromium enrichment, and to correlate these features with the electrochemical response of the textured surfaces.

Supplementary Materials: The following supporting information can be downloaded at https://www.mdpi.com/article/10.3390/eng7080404/s1. Supplementary Material S1: Raw data from the electrochemical test. Supplementary Material S2: Raw data from the microhardness measurements.

Author Contributions: Conceptualization, J.C.L.-M. and A.V.-V.; methodology, J.C.M.-R.; software, J.C.L.-M.; validation, J.C.M.-R.; formal analysis, J.C.L.-M. and C.J.-M.; investigation, J.C.L.-M. and C.J.-M.; resources, J.C.M.-R. and A.V.-V.; writing—original draft preparation, J.C.L.-M.; writing—review and editing, J.C.M.-R. and C.J.-M.; visualization, A.V.-V.; supervision, C.J.-M.; funding acquisition, J.C.M.-R. All authors have read and agreed to the published version of the manuscript.

Funding: This research received no external funding.

Institutional Review Board Statement: Not applicable.

Informed Consent Statement: Not applicable.

Data Availability Statement: The original contributions presented in this study are included in the article and Supplementary Materials. Further inquiries can be directed to the corresponding author.

Acknowledgments: We are grateful for the collaboration of the European project 2023-1-RO01-KA220-HED-000159985: Smart Healthcare Engineering (SHEng).

Conflicts of Interest: The authors declare no conflicts of interest.

References

1. Shannon, M.A.; Bohn, P.W.; Elimelech, M.; Georgiadis, J.G.; Marinas, B.J.; Mayes, A.M. Science and technology for water purification in the coming decades. *Nature* **2008**, *452*, 301–310. [CrossRef] [PubMed]
2. Elimelech, M.; Phillip, W.A. The future of seawater desalination: Energy, technology and the environment. *Science* **2011**, *333*, 712–717. [CrossRef] [PubMed]
3. Jones, E.; Qadir, M.; van Vliet, M.T.H.; Smakhtin, V.; Kang, S.M. The state of desalination and brine production: A global outlook. *Sci. Total Environ.* **2019**, *657*, 1343–1356. [CrossRef]
4. Greenlee, L.F.; Lawler, D.F.; Freeman, B.D.; Marrot, B.; Moulin, P. Reverse osmosis desalination: Water sources, technology and today's challenges. *Water Res.* **2009**, *43*, 2317–2348. [CrossRef] [PubMed]
5. Tahchieva, A.B.; Llorca-Isern, N.; Cabrera, J.M. Duplex and super duplex stainless steels: Microstructure and property evolution by surface modification processes. *Metals* **2019**, *9*, 347. [CrossRef]
6. Ma, C.; Du, Z.; Wang, X.; Zhou, P.; Zhao, Y.; Hua, Y.; Su, C.; Zhang, T.; Wang, F. Corrosion of stainless steels and corrosion protection strategies in the semiconductor manufacturing industry: A review. *Corros. Rev.* **2024**, *42*, 127–161. [CrossRef]
7. Khan, M.; Al-Absi, R.S.; Khraisheh, M.; Al-Ghouti, M.A. A better understanding of seawater reverse osmosis brine: Characterizations, uses and energy requirements. *Case Stud. Chem. Environ. Eng.* **2021**, *4*, 100165. [CrossRef]
8. Frankel, G.S. Pitting corrosion of metals: A review of the critical factors. *J. Electrochem. Soc.* **1998**, *145*, 2186–2198. [CrossRef]
9. Luo, J.; Li, X.; Cheng, Y.F. Investigation of corrosion behavior of duplex stainless steel in chloride environments. *Eng. Fail. Anal.* **2023**, *151*, 107355. [CrossRef]
10. Newman, R.C. 2001 W.R. Whitney Award Lecture: Understanding the corrosion of stainless steel. *Corrosion* **2001**, *57*, 1030–1041. [CrossRef]
11. Macdonald, D.D. Reflections on the history of electrochemical impedance spectroscopy. *Electrochim. Acta* **2006**, *51*, 1376–1388. [CrossRef]
12. Cojocaru, E.M.; Nocivin, A.; Răducanu, D.; Angelescu, M.L.; Cinca, I.; Balkan, I.V.; Șerban, N.; Cojocaru, V.D. Microstructure Evolution during Hot Deformation of UNS S32750 Super-Duplex Stainless Steel Alloy. *Materials* **2021**, *14*, 3916. [CrossRef] [PubMed]
13. Kim, D.; Kim, K.; Park, J.; Chung, W.; Shin, B.-H. Microstructure and corrosion performance of high-entropy alloy, austenitic stainless steel and super duplex stainless steel in 3.5 wt.% NaCl solution. *Int. J. Electrochem. Sci.* **2023**, *18*, 100074. [CrossRef]
14. Davidson, K.P.; Liu, R.; Zhu, C.; Cagirici, M.; Tan, L.P.; Alagesan, A.; Singamneni, S. Effect of build orientation and heat treatment on the microstructure, mechanical and corrosion performance of super duplex stainless steels fabricated via laser powder bed fusion. *Mater. Adv.* **2024**, *5*, 8177–8198. [CrossRef]
15. Yu, C.; Sasic, S.; Liu, K.; Salameh, S.; Ras, R.H.A.; van Ommen, J.R. Bio-inspired drag reduction: From natural organisms to artificial functional surfaces. *Giant* **2020**, *2*, 100017. [CrossRef]
16. Ahmad, A.; Xirouchakis, P.; Pearson, A.; Brownlie, F.; Gorash, Y. Development of laser AM process to repair damaged super duplex stainless steel components. *Sustainability* **2025**, *17*, 5438. [CrossRef]
17. Camerini, C.G.; Silva, V.M.A.; Soares, I.A.; Santos, R.W.F.; Ramos, J.E.; Santos, J.M.C.; Pereira, G.R. Ferrite content meter analysis for delta ferrite evaluation in super duplex stainless steel. *J. Mater. Res. Technol.* **2018**, *7*, 366–370. [CrossRef]
18. Hersen, P.; Andersen, K.H.; Elbelrhiti, H.; Andreotti, B.; Claudin, P.; Douady, S. Corridors of barchan dunes: Stability and size selection. *Phys. Rev. E* **2004**, *69*, 011304. [CrossRef] [PubMed]
19. Andreotti, B.; Claudin, P.; Pouliquen, O. Selection of dune shapes and velocities. *Eur. Phys. J. B* **2002**, *28*, 321–339. [CrossRef]
20. Liu, S.; Chen, Y.; Zhang, Q.; Yu, T. Pitting corrosion resistance of annealing-treated super duplex stainless steel S32750. *Crystals* **2020**, *10*, 294. [CrossRef]
21. Liu, M.; Du, C.; Liu, Z.; Li, X.; Wang, L.; Zhong, R.; Cheng, X.; Ao, J.; Duan, T.; Zhu, Y.; et al. A review on pitting corrosion and environmentally assisted cracking of duplex stainless steel. *Microstructures* **2023**, *3*, 2023026. [CrossRef]

22. Ince, F.D.; Özel, T. Laser surface texturing of materials for surface functionalization: A holistic review. *Surf. Coat. Technol.* **2025**, *498*, 131818. [CrossRef]
23. Sun, Q.; Xie, F.; Zhang, Y.; Wang, D.; Wu, M. Stability of passive film and pitting susceptibility of 316L stainless steel in the aggressive oilfield environment containing Cl−–CO2–O2. *Electrochim. Acta* **2024**, *499*, 144709. [CrossRef]
24. Bozkurt, Y.B.; Kavasoğlu, Y.S.; Atik, B.; Tüzemen, S.M.; Kovacı, H.; Çelik, A. Optimization of surface texture geometry for enhanced tribocorrosion resistance in additively manufactured AISI 316L stainless steel. *Electrochim. Acta* **2026**, *554*, 148304. [CrossRef]
25. Ahuir-Torres, J.I.; Al-Mahdy, A.; Sharp, M.C.; Opoz, T.T.; Zhu, G.; Bashir, M.; Kotadia, H.R. The influence of texture density and free surface energy on the corrosion resistance of laser-textured 316L stainless steel. *npj Mater. Degrad.* **2025**, *9*, 115. [CrossRef]
26. Ahmed, F.; Chamorro, L.P. On Bio-Inspired Strategies for Flow Control, Fluid–Structure Interaction, and Thermal Transport. *Biomimetics* **2026**, *11*, 143. [CrossRef] [PubMed]
27. Pou, P.; del Val, J.; Riveiro, A.; Comesaña, R.; Arias-González, F.; Lusquiños, F.; Bountinguiza, M.; Quintero, F.; Pou, J. Laser texturing of stainless steel under different processing atmospheres: From superhydrophilic to superhydrophobic surfaces. *Appl. Surf. Sci.* **2019**, *475*, 896–905. [CrossRef]
28. Sayyar, N.; Hansen, V.; Tucho, W.M.; Minde, M.W. Directed laser deposition of super duplex stainless steel: Microstructure, texture evolution and mechanical properties. *Heliyon* **2023**, *9*, e15144. [CrossRef] [PubMed]
29. Bonse, J.; Höhm, S.; Kirner, S.V.; Rosenfeld, A.; Krüger, J. Laser-induced periodic surface structures—A scientific evergreen. *IEEE J. Sel. Top. Quantum Electron.* **2017**, *23*, 9000615. [CrossRef]
30. Al-Mahdy, A.; Kotadia, H.R.; Sharp, M.C.; Opoz, T.T.; Mullett, J.; Ahuir-Torres, J.I. Effect of surface roughness on the surface texturing of 316L stainless steel by nanosecond pulsed laser. *Lasers Manuf. Mater. Process.* **2023**, *10*, 141–164. [CrossRef]
31. Moldovan, E.R.; Concheso-Doria, C.; Ocaña, J.L.; Baltes, L.S.; Stanciu, E.M.; Croitoru, C.; Pascu, A.; Roată, I.C.; Tîrău, M.H. Wettability and surface roughness analysis of laser surface texturing of AISI 430 stainless steel. *Materials* **2022**, *15*, 2955. [CrossRef] [PubMed]
32. Alencar, L.M.; Falcão, S.S.; de Melo, H.G.; de Castro, R.S.; Bugarin, A.F.S.; dos Santos, R.G.; Terdad, M.; Suegama, P.H. The influence of laser surface texturing parameters on the surface of lean duplex stainless steel 2101: Microstructure and corrosion properties. *Surf. Coat. Technol.* **2025**, *518*, 132908. [CrossRef]
33. Liu, N.; Zhou, Q.; Xu, M.; Niu, M.; Zhou, P.; Guo, P. Evolution in microstructure and properties of laser-cladded CoCrFeMoNi coatings at different annealing temperatures. *Mater. Sci. Technol.* **2023**, *39*, 2782–2791. [CrossRef]
34. Xu, Y.; Li, W.; Zhang, S.; Wang, J. A short review of medical-grade stainless steel: Corrosion resistance and novel techniques. *J. Mater. Res. Technol.* **2024**, *29*, 2788–2798. [CrossRef]
35. *ASTM E384-22*; Standard Test Method for Microindentation Hardness of Materials. ASTM International: West Conshohocken, PA, USA, 2022.
36. *ISO 10271:2020*; Dentistry—Corrosion Test Methods for Metallic Materials. International Organization for Standardization: Geneva, Switzerland, 2020.
37. *ASTM G102-23*; Standard Practice for Calculation of Corrosion Rates and Related Information from Electrochemical Measurements. ASTM International: West Conshohocken, PA, USA, 2023.
38. *ISO 16773-1:2016*; Electrochemical Impedance Spectroscopy (EIS) on Coated and Uncoated Metallic Specimens—Part 1: Terms, Definitions and Test Conditions. International Organization for Standardization: Geneva, Switzerland, 2016.
39. Moura, V.S.; Lima, L.D.; Pardal, J.M.; Kina, A.Y.; Corte, R.R.A.; Tavares, S.S.M. Influence of microstructure on the corrosion resistance of duplex stainless steel UNS S31803. *Mater. Charact.* **2008**, *59*, 1127–1132. [CrossRef]
40. Tan, H.; Jiang, Y.; Deng, B.; Sun, T.; Xu, J.; Li, J. Effect of annealing temperature on the pitting corrosion resistance of super duplex stainless steel UNS S32750. *Mater. Charact.* **2009**, *60*, 1049–1054. [CrossRef]
41. Pecly, P.H.R.; Mendes, I.C.; Pimenta, A.R.; Oliveira, A.L.C.; Felix, V.D.S.; Beraldo, H.; Rocha Junior, N.T. Microstructure, corrosion resistance and hardness of the simulated heat-affected zone of duplex UNS S32205 and super duplex UNS S32750 stainless steels. *J. Mater. Eng. Perform.* **2023**, *32*, 9019–9030. [CrossRef]

Disclaimer/Publisher's Note: The statements, opinions and data contained in all publications are solely those of the individual author(s) and contributor(s) and not of MDPI and/or the editor(s). MDPI and/or the editor(s) disclaim responsibility for any injury to people or property resulting from any ideas, methods, instructions or products referred to in the content.